Bouich, A.; Cerutti Torres, J.; Chfii, H.; Marí-Guaita, J.; Khattak, YH.; Baig, F.; Marí, B.... (2023). Delafossite as hole transport layer a new pathway for efficient perovskite-based solar sells: Insight from experimental, DFT and numerical analysis. Solar Energy. 250:18-32. https://doi.org/10.1016/j.solener.2022.12.022

Delafossite as Hole Transport Layer a New Pathway for Efficient Perovskite-based Solar Sells: Insight from Experimental, DFT and Numerical Analysis

Amal Bouich[1,2], Joeluis Cerutti Torres[4], Hasnae Chfii[1,5], Julia Marí-Guaita[1], Yousaf Hameed Khattak[1,3], Faisal Baig[1,3], Bernabé Marí Soucase[1], Pablo Palacios[2,4,*]

[1]Escuela Técnica Superior de Ingeniería del Diseño: Universitat Politècnica de València, València, Spain.

[2]Instituto de Energía Solar, ETSI Telecomunicación, Universidad Politécnica de Madrid, Ciudad Universitaria, Madrid, Spain

[3]Electrical Engineering Department, Federal Urdu University of Arts, Sciences and Technology, Islamabad, Pakistan

[4]Dept. Física Aplicada a las Ingenierías Aeronáutica y Naval. ETSI Aeronáutica y del Espacio, Universidad Politécnica de Madrid, Pz. Cardenal Cisneros, 3, 28040 Madrid, Spain

[5]University Mohamed V Rabat-Marocco

Corresponding Author: * ambo1@doctor.upv.es, bmari@fis.upv.es, pablo.palacios@upm.es

Abstract:

Herein, we propose a successful technique to produce delafossite materials that can be applied as Hole Transport Layer (HTL) in inorganic lead halide Perovskite solar cells (PSCs). The delafossite $CuMO_2$, where $M = Al, Ga, Fe, Cr, Ni, Co, Cr$ types were investigated the M cation effect on the crystal structure, morphology, and optical properties. These properties were investigated using x-ray, scanning electron microscopy (SEM), transmission electron microscopy (TEM), and UV visible spectroscopy. The XRD results confirmed their hexagonal and rhombohedral-like structure, where the SEM image of $CuMO_2$ shows the good formation of delafossite layers. The optical band gap of $CuMO_2$ varies from 2.2eV to 2.99eV, which is well in line with the literature. Similarly, we also perform the density functional theory (DFT) calculations for delafossite layers to find their electronic properties of them. Based on experimental and DFT calculations, we performed the numerical analysis in SCAPS-1D software on standard solar cell structure ($Spiro-OMeTAD\ /\ MAPbI_3\ /\ TiO_2$) and replaced $Spiro-OMeTAD$ with all the deposited delafossite layers. Our numerical analysis found that HTL shows the highest power conversion efficiency (PCE%) of 22.90. The proposed work can give a good direction for manufacturing to improve the performance of Perovskite-based solar cells (PSCs).

Keywords: Delafossite, $CuMO_2$, HTL, PSCs, Morphology, optical properties, perovskite, solar cells, DFT, HSE06

1. Introduction:

There has been considerable interest in organic-inorganic metal halide perovskite solar cells (PSCs) in recent years because of their excellent photophysical properties [1]–[4] such as high absorption coefficients ($> 10^5\ cm^{-1}$) [5]–[7], long diffusion lengths, and high charge carrier mobility ($> 100\ cm^2/Vs$). As a result, over 25% of power is converted into electrical energy [5], [8]–[10]. TiO_2 and spiro-OMeTAD have been used as electron transport layer (ETL) and hole transport layer (HTL) in most PSCs. It is however very costly and unstable under soaking, thermal stress, and/or humid conditions, making these organic-based HTL costs prohibitive and limiting their lifetime [11]. Eco-friendly delafossite material structures are optically transparent in the visible region, having an energy band gap greater than 3.1eV [12]–[15]. Since optically transparent materials typically have a large bandgap, they tend not to conduct electricity. On the other hand, TCOs are a class of materials that exhibit both electrical conductivity ($10^4 Scm^{-1}$) and transparency in the visible range (90%), Delafossite ternary oxides have the chemical formula ABO_2 [13], where A is usually copper (Cu^+) or silver (Ag^+) in a monovalent state, and B is a trivalent metal (M^{+3}) such as chromium (Cr^{+3}), Cobalt (Co^{+3}), aluminum (Al^{+3}), gallium (Ga^{+3}), copper (Ag^{+3}), iron (Fe^{+3}), manganese (Mn^{+3}). Almost all TCOs fabricated are n-type semiconductors and play a very important role as transparent electrodes. Substitutional doping or inducing non-stoichiometry in the material induces holes in a p-type conductor's valence band [16], [17]. Before using any of the previous delafossite, a study made to know their suitable work function, preferable electronic properties, and especially their stability [18], [19]. Delafossite $CuMO_2$ where $M = Al, Ga, Fe, Cr, Ni, Co$ has a rhombohedral/ hexagonal symmetry of O-M-O and MO_6 layers [17]. Copper-based delafossite oxides are the focus of many reports including $CuFeO_2$ [20]–[22] $CuCrO_2$ [23], $CuGaO_2$ [24] and $CuAlO_2$ [25] already have been intensively investigated. According to the literature, few papers were published on the $CuMO_2$ delafossite. This made us to ask the question of which delafossite $CuMO_2$ where $M = Al, Ga, Fe, Cr, Ni, Co$ can be trusted to use in an application as HTL in perovskite solar cells.

So, in this work, we proposed a spin coating technique for successfully depositing delafossite materials and performing characterization studies such as x-rays diffraction, SEM, TEM, and optical band gap of delafossite materials. Next, we find the electrical properties of these materials via density functional theory (DFT) and based on our experimental and computational findings we apply numerical analysis techniques to find the suitability of those materials for application of hole transport layers. Numerical analysis was performed in solar cell capacitance software (SCAPS-1D) developed by the University of Gent, Belgium [26]–[33]. SCAPS-1D has been extensively used for numerical analysis of perovskite and kesterite thin film solar cells in the last few years [33]–[39]. In our work SCAPS-1D was used to analyze the performance of perovskite

solar cell structure $Spiro - OMeTAD\ /\ MAPbI_3\ /\ TiO_2$. The $Spiro - OMeTAD$ was replaced with delafossite materials to be used as HTL.

2. Experimental:

2.1. Materials:

Unless specified otherwise, all the chemicals in these experiments were purchased from Alfa Aesar or Sigma-Aldrich with analytical grade and used without further purification.

2.2. Delafossite Manufacture:

The delafossite films were prepared by one-step spin coating. In the first step, deionized water was used to dissolve 20 mmol of copper (II) nitrate hemi pentahydrate and 20 mmol of M (III) chloride hexahydrate where M can be Al, Co, Ni, Fe, Ga, Cr, A homogeneous colloidal suspension was obtained by adding 5.8 g of sodium hydroxide in aqueous solution to the above solution (70 mL total volume). In the following step, the brownish solution was placed in a spin coating.

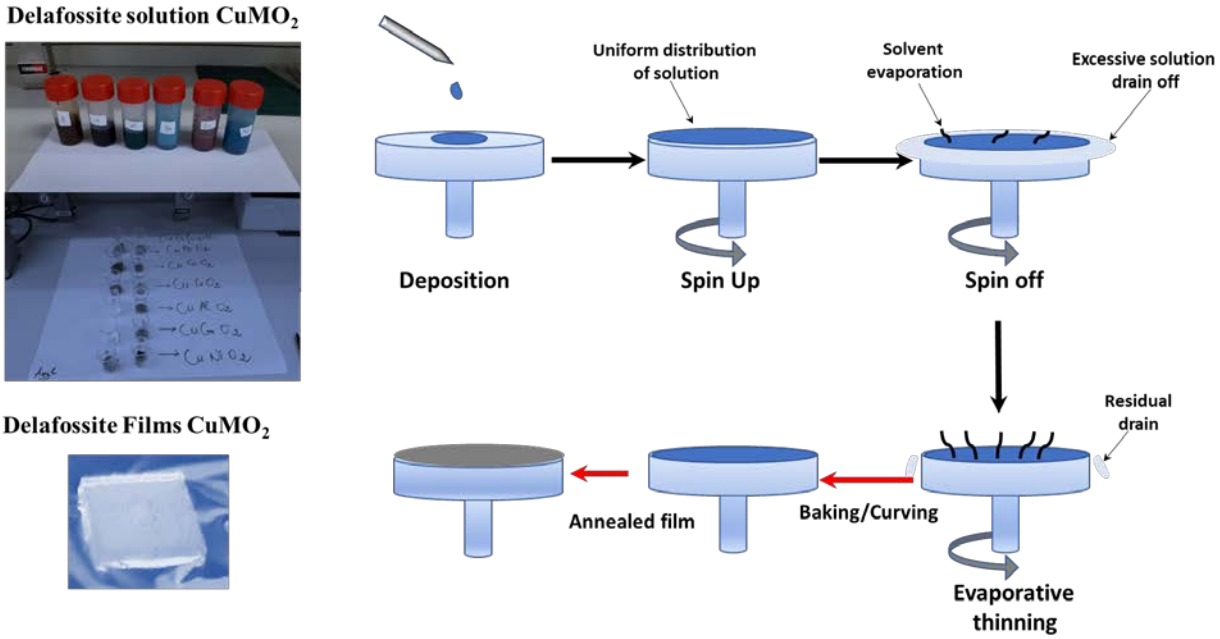

Figure 1: Synthesis of delafossite $CuMO_2$ where $M = Al, Co, Ni, Fe, Ga, Cr$ by spin coating technique.

2.3. Characterization Techniques:

Diffractometry system = XPERT-PRO is the X-ray Diffraction monochromator used to establish the structural characterization of the samples with a wavelength of 0.15406 nm, 20 kV and Cu-Kα radiation. We obtained the measurements based on Bragg's law. Scanning electron microscopy (SEM) was used to identify the surface morphology of the powders at 25kV as an acceleration voltage. Using a fiber linked optical microscope, the sample was targeted by the He-Cd laser (442 nm) at 100× magnification. We are interested in the wavelength of 400–800 cm^{-1} range. A high-resolution 100 kV (TEM 100) Transmission Electron Microscope was used to perform additional structural analysis. Its conditions of measurement were 2.5 kV at several magnifications.

2 Results and discussion:

The $CuMO_2$ $(M = Al, Fe, Co, Ga, Ni, Cr)$ Delafossite films prepared by the spin coating [25] method were characterized by X-Ray diffraction [24]. Each diffractogram presents the existence of both the delafossite and FTO peaks, Figure. 2 mentions the hkl of the phase's peaks where the delafossite $CuAlO_2$has (104) as the highest intensity, which is located at 2Θ=38°, $CuCrO_2$ has (004) as the highest intensity which is located at 2Θ=27°, for the $CuNiO_2$ delafossite gave us a result which is not far from the previous one, the copper-iron oxide $CuFeO_2$is as well as the $CuGaO_2$ delafossite (Figure 2-E) and $CuCoO_2$(Figure 2-B) diffractograms having the phases peaks, (310) at 2Θ=35°, (101) at 2Θ=37,8°, and (200) at 2Θ=37,6° respectively.

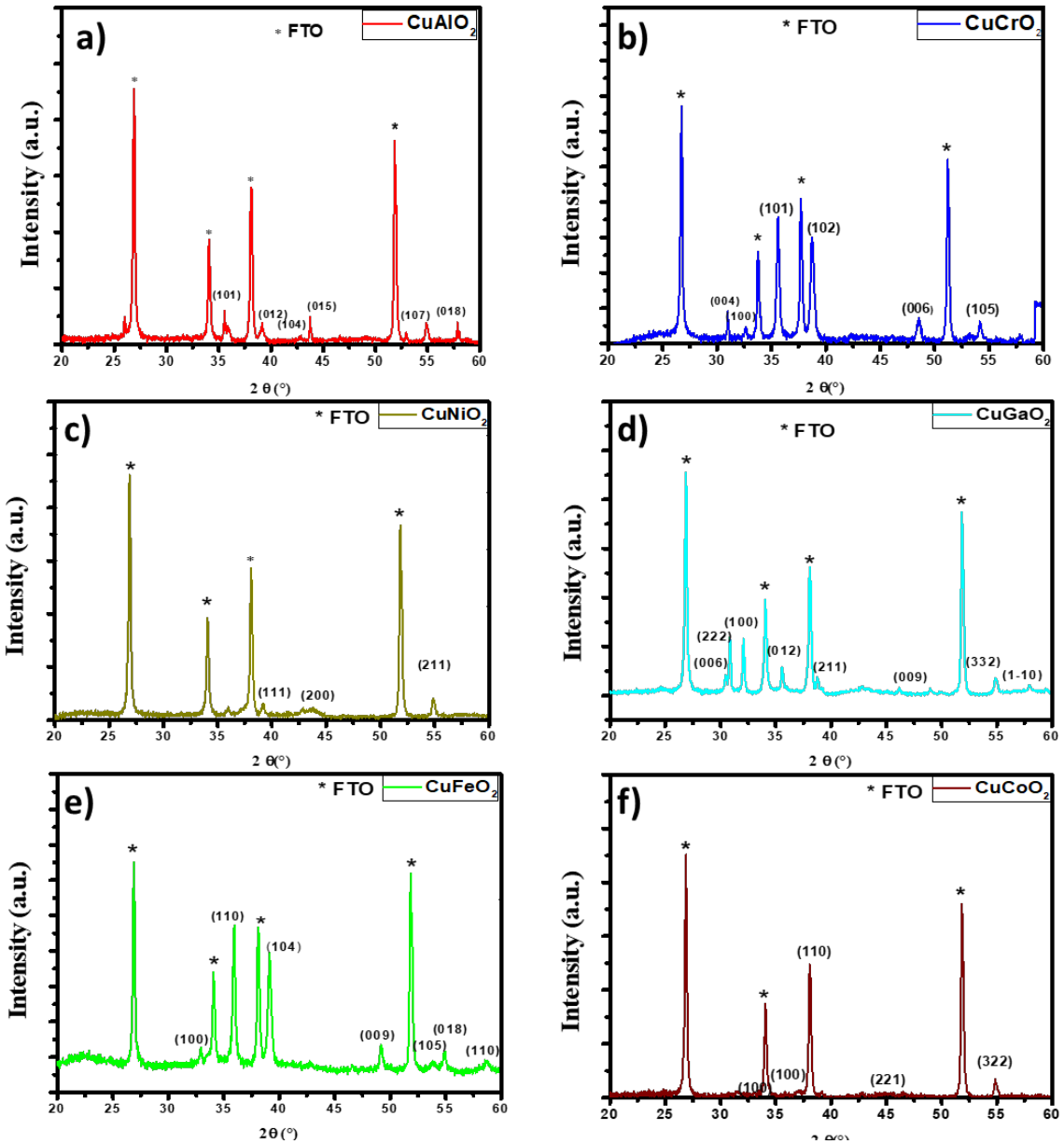

Figure 2: The XRD pattern of the single-phase $CuMO_2$ where $M = Al, Co, Ni, Fe, Ga, Cr$.

Figure 2 shows the XRD pattern of the single-phase $CuMO_2$ where $M = Al, Ga, Fe, Cr, Ni,$ Co, the diffractograms indicate the existence of both the delafossite peaks and the FTO peaks. FTO is indicated by stars in all the graphs. The $CuAlO_2$ pattern was well defined where the peaks: (101),

(012), (104), (107), and (018) (Figure 2-A) are referenced to the database JCPDS card No 74-2361 and located at 36,22°; 37,40°; 41,81°; 52,38°; and 56,70 respectively. It appears that in $CuAlO_2$ the film is randomly oriented based on the XRD results. Figure 2-B indicates the pattern of the $CuCoO_2$ containing both the delafossite phase and FTO peaks (based on the database JCPDS card No. 074-1855) (222) at $2\Theta=31{,}26°$, (100) at $2\Theta=36{,}77°$, (110) at $2\Theta=37{,}91°$, (211) at $2\Theta=42{,}22°$, and (332) at $2\Theta=56{,}84°$.

For $CuNiO_2$, (Figure 2-C) the database JCPDS card No. 006-0720 is the reference that had been based on to identify the copper-nickel oxide's peaks, those last are: (111), (002), and (200) located at 37,01°; 41,34°; and 43,80° respectively. Figure 2-E is the diffractogram corresponding to the $CuGaO_2$ delafossite based on the card of the database JCPDS No. 035-1402 [40], [41], the sample contains: (006), (101), and (009) at 31,27°; 35,22°; and 47,67° respectively. Four peaks appeared of the $CuFeO_2$ delafossite which have the planes hkl: (006), (012), (009), and (105), situated at the $2\Theta=31{,}23°$; 35,69°; 47,64°; and 55,21° respectively [42]–[44].

Figure 2-F shows the XRD patterns of $CuCrO_2$. The diffractogram mentioned the peaks referenced to the reference JCPDS card No 089-0540 [45]: (004), (101), (102), (103), (006), and (105) that are located at: 31,36°; 35,75°; 38,36°; 42,40°; 47,83°; and 53,67° respectively. The diffraction pattern showed peaks for $CuCrO_2$, as well as for FTO-covered substrates. Diffraction patterns did not show any other reflections that could have been indicative of diffusion between the different layers, such as reflections from another compound containing Cu and Cr. Comparing to the six types of delafossite, the $CuAlO_2$ is the good one that can give us a result with an excess of the phase peaks. All peaks arose from $CuAlO_2$ delafossite, no diffraction peaks of $Cu(NO_2)_3$ and $NaAlO_2$ appeared in the patterns of the products obtained. Possibly due to the very small grain sizes (Table 1), the peaks of the nanocrystal diffraction pattern were more intense than those in the film pattern.

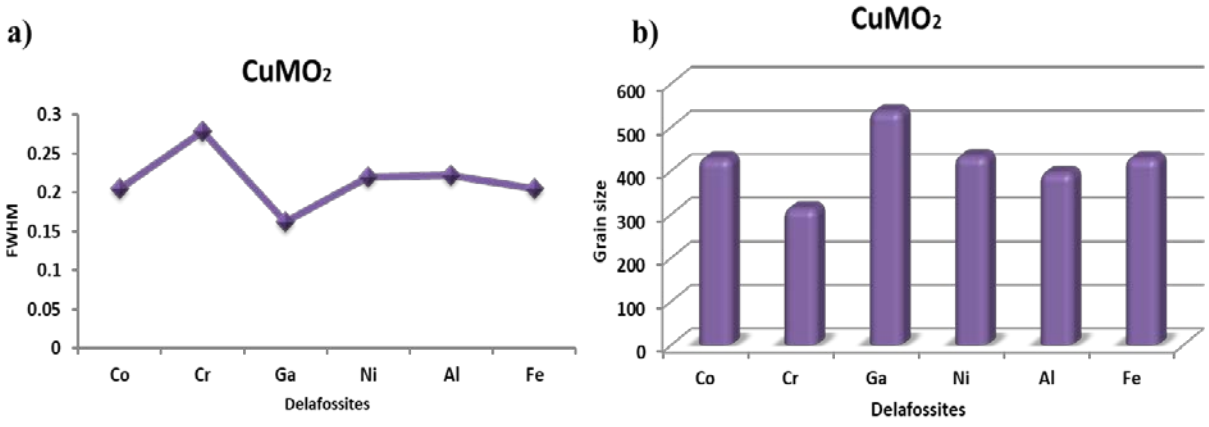

Figure 3: FWHM and grain size for the characteristic peaks in terms of the $CuMO_2$ delafossite

Table 1: A summary of both Grain size and FWHM corresponding to six different $CuMO_2$ delafossite

$CuMO_2$	**$CuCoO_2$**	**$CuCrO_2$**	**$CuGaO_2$**	**$CuNiO_2$**	**$CuAlO_2$**	**$CuFeO_2$**
2θ	38.070	35.928	35.554	54.844	38.088	35.938
FWHM (°)	0.205	0.279	0,162	0.22	0.222	0.205
Grain size (nm)	428	313	536	433	395	428

The film's crystallite size (D) was calculated by Scherer's equation (1):

$$D = \frac{\lambda K}{\beta cos\theta} \quad (1)$$

Where:

λ = Wavelength (0.1540 nm),

k = Scherer's constant (0.9), θ = Bragg's diffraction angle,

β = FWHM (Full-Width at half maximum),

To have an idea about the deformations and the imperfections of the grains in the level of the films synthesized, Lattice strain (ε) [46]can help us with the following equation 2.

$$\delta = \frac{1}{D^2} \quad (2)$$

From calculations of X-ray diffraction data (XRD), we can have more precision on a specific area of the powders by the dislocation density (δ) [47], [48]. It was evaluated using the following formula: 3.

$$\varepsilon = \frac{\beta}{4tan\,\theta} \quad (3)$$

We summarized the obtained results in Table 2.

Table 2: The average crystallite size (D), dislocation density (δ), and lattice strain function (ε) of the characteristic peaks

Samples ID	**2θ**	**B** $(FWHM)$	**D** (nm)	**δ** $(nm)^{-2}$	**ε**
$CuAlO_2$	38.16	0.180	0.173	33.41	0.161
$CuCoO_2$	37.56	0.193	0.758	1.740	0.141
$CuNiO_2$	31.16	0.180	0.173	33.41	0.161
$CuFeO_2$	36.77	0.181	0.806	1.539	0.136
$CuGaO_2$	35.74	0.117	1.248	0.642	0.088
$CuCrO_2$	35.77	0.181	0.806	1.539	0.136

The Full-Width at half maximum shows close values between the two characteristic peaks of each growth delafossite, the good results are given by $CuMO_2$ where $M = Al, Ga$ unlike delafossite the rest $CuMO_2$ where $M = Fe, Cr, Ni, Co$ and this is due to the good crystallinity Figure 3.

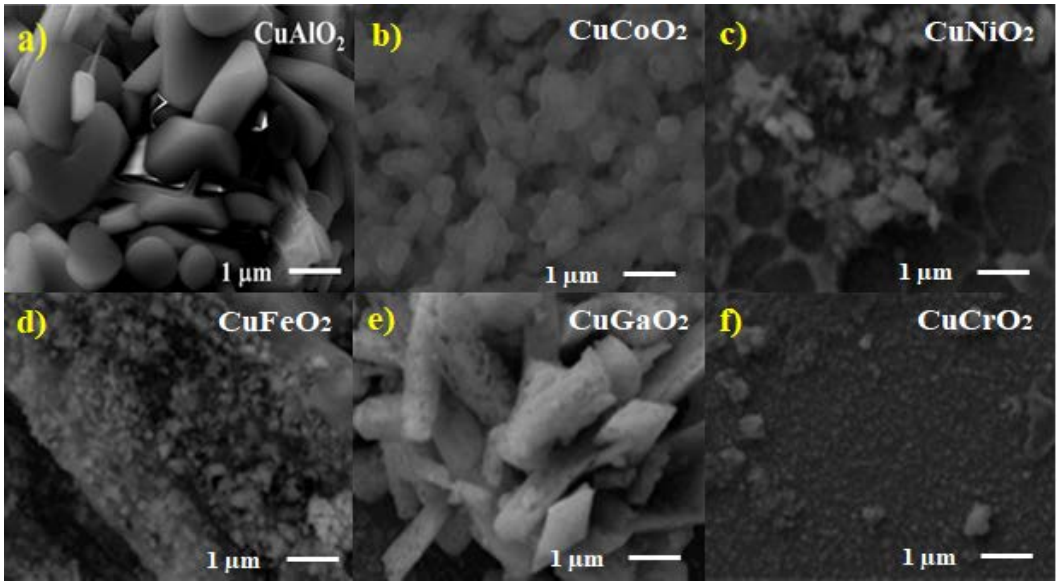

Figure 4: SEM images of $CuMO_2$ where $M = Al, Co, Ni, Fe, Ga, Cr$.

Scanning electron microscopy (SEM) was used to identify the surface morphology of the powders at 25kV as an acceleration voltage [49]–[51]. Figure 4 depicts SEM's results indicating the morphology of the surface of all the samples $CuMO_2$ where $M = Al, Ga, Fe, Cr, Ni, Co$. By changing the cation M, the body type normally changes between different shapes, from the small grains of $CuCrO_2$ (Figure 4-f) to the bigger ones of $CuGaO_2$ (Figure 4-e). The histogram confirms this observation in Figure 3. It clearly showed that the $CuAlO_2$ delafossite gave the best result compared to the other samples, where the scan was a picture of shapes of poles intertwined with each other, clear and, white due to its reception machine's light.

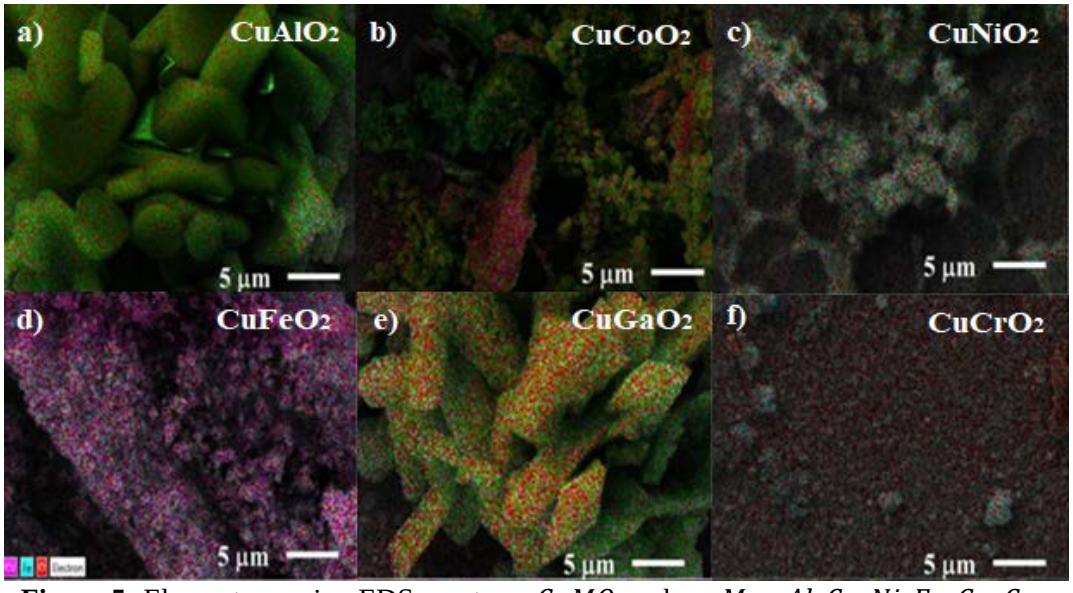

Figure 5: Element mapping EDS spectrum $CuMO_2$ where $M = Al, Co, Ni, Fe, Ga, Cr$.

The chemical composition of the delafossite was analyzed by energy-dispersive X-ray spectroscopy (SEM-EDX) mapping to characterize the films $CuMO_2$ where $M = Al, Ga, Fe, Cr, Ni, Co$. The images in Figure 5a-f show the containing elements of a specific selected area. Furthermore, the homogeneity of the samples can be observed such that all the elements are distributed in the whole substrates' areas; To know the name of these elements, we

mapped the delafossite in Figure 6. This Figure shows the compounds of the six substrates and their positions exactly in the sample to ensure the copper-M-oxide elements. This mapping confirms the scanning electron microscopy (SEM) results.

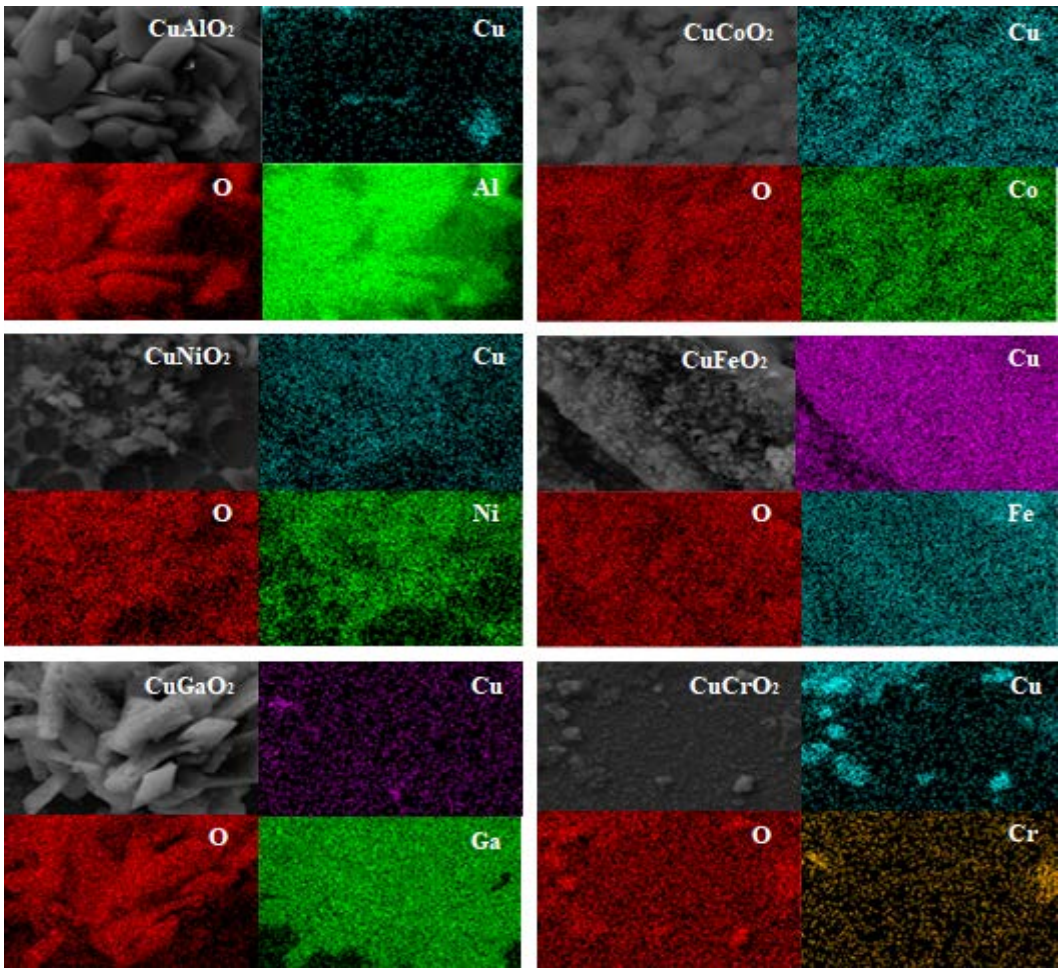

Figure 6: Element mapping $CuMO_2$ where M= Al, Co, Ni, Fe, Ga, Cr.

Figure 7 shows a TEM analysis of $CuMO_2$ thin film monocrystal with lattice fringe spacing of 0.17 nm corresponding to (110) or (220) of the $CuMO_2$ phase. This result has already been confirmed by the XRD pattern (Figure.7), where Figure shows the selected area of the electron diffraction spectrum, revealing that $CuMO_2$ thin films are polycrystalline.

The TEM revealed no second phase in a fully reacted sample. An image of the $CuAlO_2$ crystal lattice in Figure 7 is shown. The $CuAlO_2$ The layer does not have any grain boundaries or other planar defects. An ion stripe line is shown in Figure 7 at intervals of 0.17 nm.

$CuCoO_2$ films were further characterized by TEM. It is easy to distinguish the hexagonal structure from other structures, as shown in Figure. $CuCoO_2$ films were observed to be between 80 and 170 nm in size.

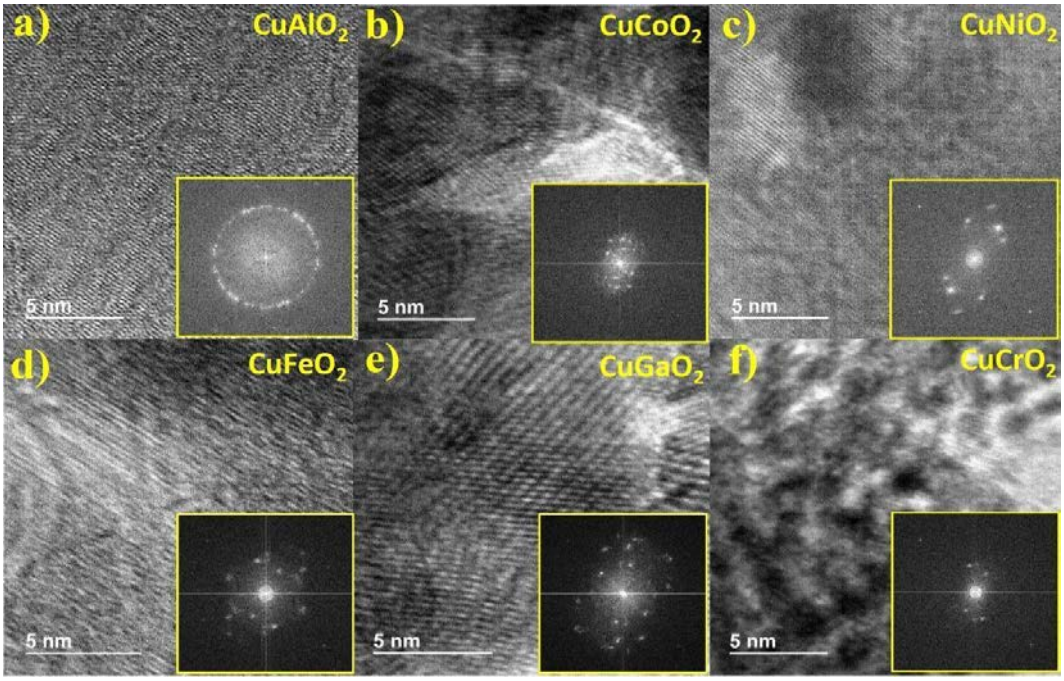

Figure 7: HRTEM image of $CuMO_2$ $where\ M = Al, Co, Ni, Fe, Ga, Cr$ taken from the substrate and 0.1m Torr O_2 pressure. Accompanied with the Fourier transforms of the data.

Figure 8 represents the AFM analysis of the $CuMO_2$ films in an area of 2 µm × 2 µm. The surface morphology and roughness vary depending on the composition of the film. Roughness has been calculated by the root-mean-square method (rms) showing dramatic changes for all different compounds. The results are summarized in Table 3. Nonetheless, the rms decreases to 36.99 nm for $CuCoO_2$ (Figure 8). The larger hills and troughs make the surface rougher in the AFM analysis. The morphology is correlated to SEM Analysis until a certain point.

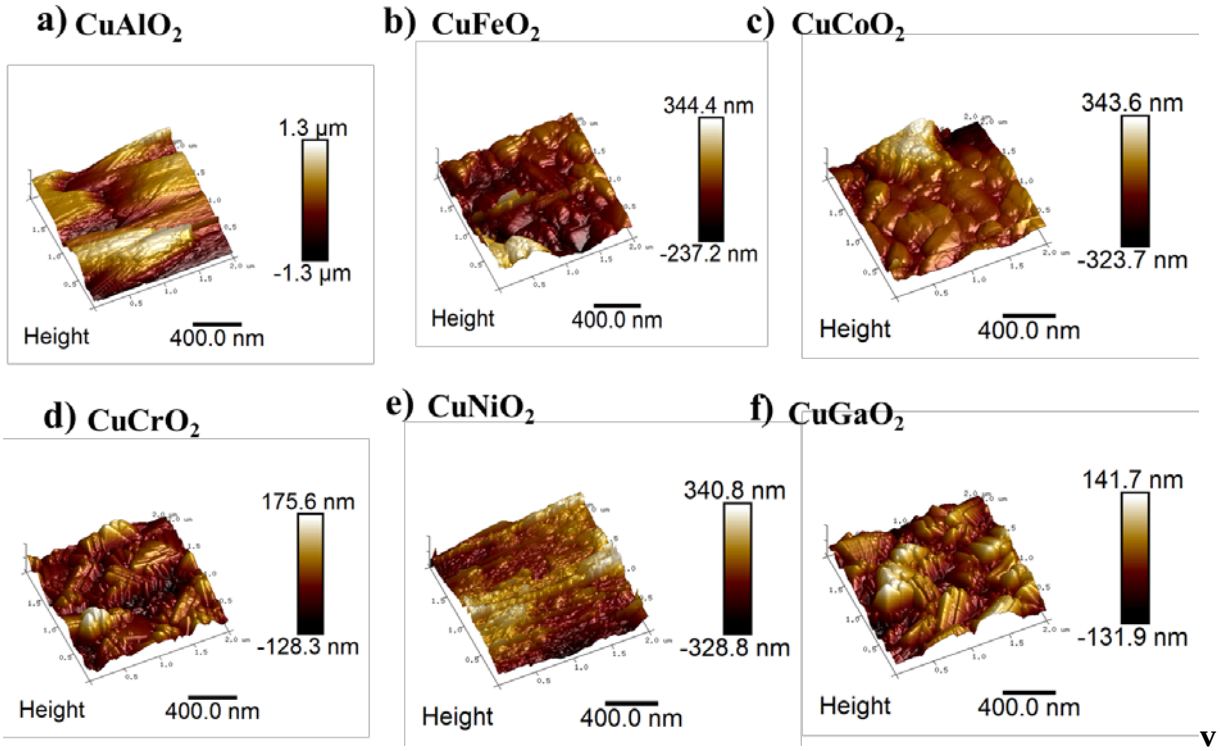

Figure 8: AFM images of $CuMO_2$ where $M = Al, Co, Ni, Fe, Ga, Cr$ in 3D

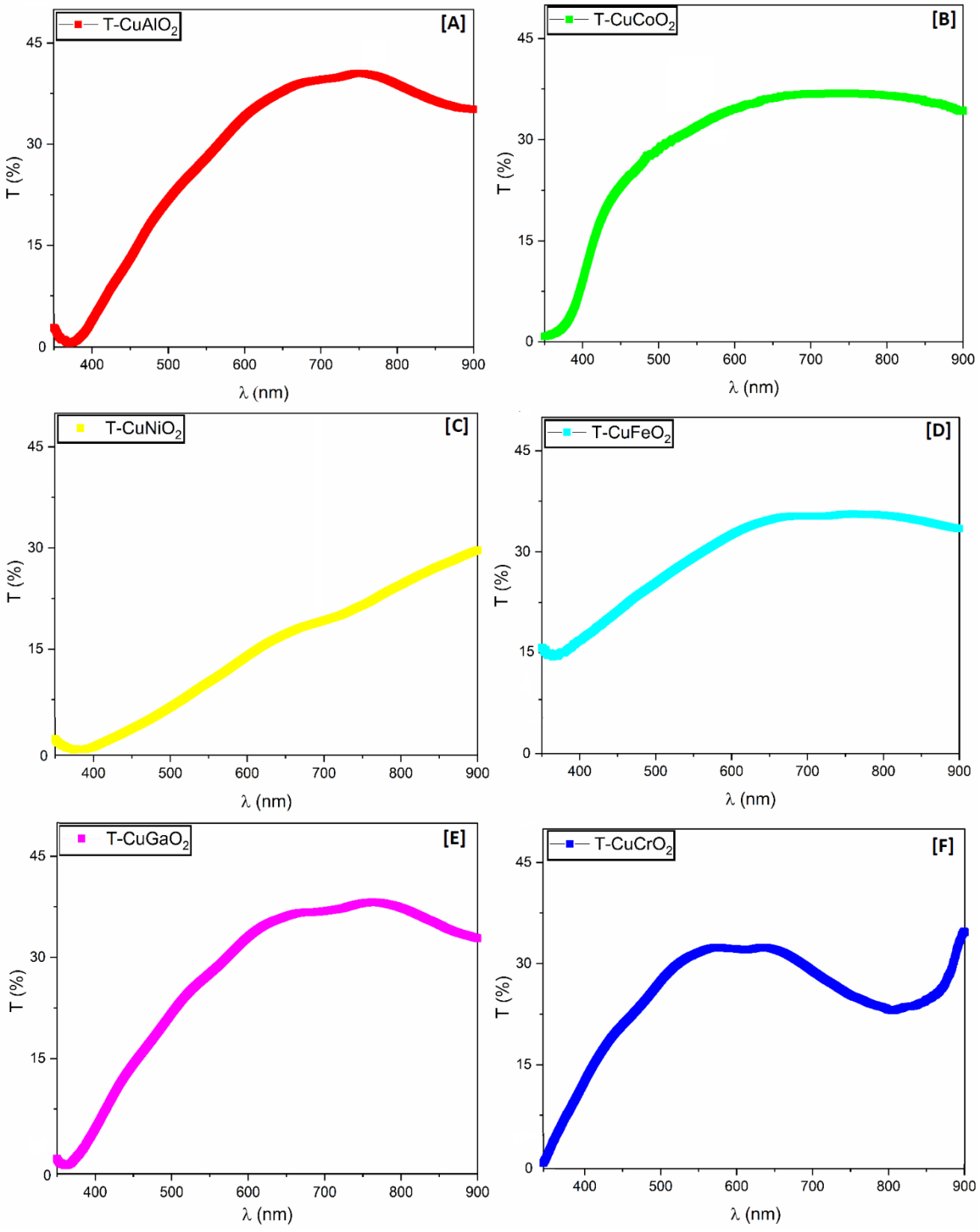

Figure 9: Transmission of $CuMO_2$ where $M = Al, Co, Ni, Fe, Ga, Cr$

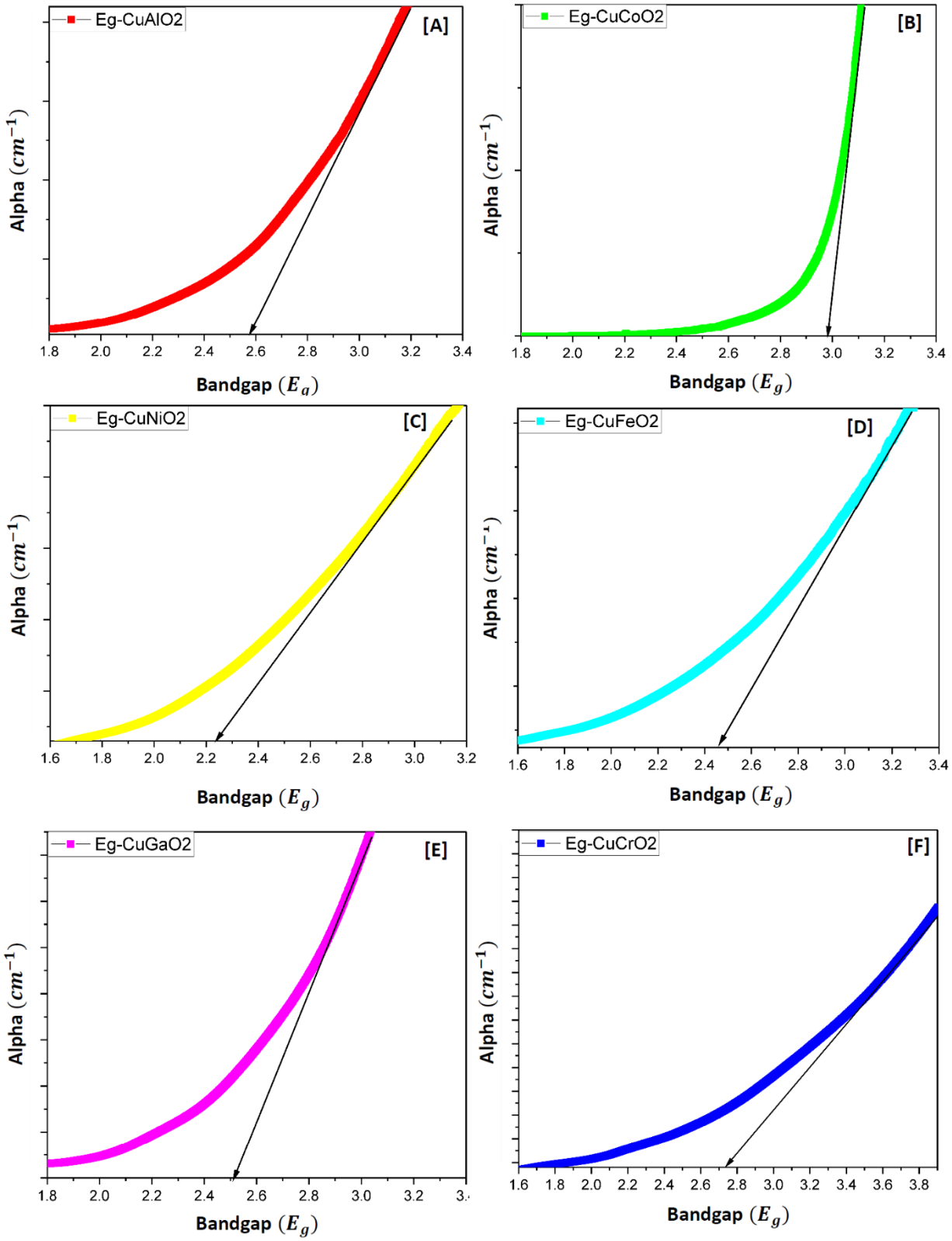

Figure 10: Band gap of the $CuMO_2$ delafossite samples where $M = Al, Co, Ni, Fe, Ga, Cr$.

We record the transmission spectra for $CuMO_2$ delafossite samples, these records are displayed in Figure 9.

As for the optical band gap Eg of the layers, they are deduced from the Tauc plots. The Tauc equation describes the evolution of $(\alpha hv)^{1/n}$ vs. hv, as follows:

$$(\alpha hv)^{1/n} = (hv - Eg) \quad (4)$$

Where:

- β a constant independent of hv.
- ''n'' depends on the type of band gap transition.

In our case the transition is direct hence n=1/2 and:

$$(\alpha hv)^2 = (hv - Eg) \quad (5)$$

The results for recorded energy gaps (pertaining to measurable absorption edges) for all the samples. We're interested in the visible range (400-800 nm). Compared to all the graphs, the one that gives the good transmission percentage is the $CuAlO_2$, where it can transmit light up to 60% in the visible range. The $CuGaO_2$ has approximately a similar transmission of around 60% between 400 and 800nm.

3 Electronic structure: theoretical simulations

First-principles calculations were performed to obtain an accurate description of the electronic structure and properties of the six delafossite-type oxides $CuMO_2$ under study and to compare the effect of the metal M on the electronic configuration $(M = Al, Co, Cr, Fe, Ga, Ni)$. For all the materials the atomic positions were optimized within the Density Functional Theory (DFT) approach, based on the framework of the generalized Kohn-Sham scheme [52], [53] in combination with the projector augmented-wave (PAW) method [54] and the Heyd-Scuseria-Ernzerhof hybrid functional with the modified fraction of screened short-range Hartree Fock exchange (HSE06) [55]–[57] as implemented in the Vienna ab initio simulation package (VASP) [58]–[60].

The modeled system $CuMO_2$ was defined through a tetragonal unit cell with 12 atoms $(Cu_3M_3O_6)$. The electronic wavefunctions were expanded in a plane wave basis setup to a kinetic energy cutoff of 400 eV , the atomic positions were optimized using the conjugate gradient method until the force on each atom was less than $0.01\ eV\text{Å}^{-1}$ and an energy convergence less than $10^{-8}\ eV$. For the Brillouin zone integration, a $12 \times 12 \times 6$ Monkhorst-Pack scheme k-point was used [61].

Figure 11 shows the arrangement of atoms for the studied materials. The delafossite structure can be appreciated fairly: an alternate stacking of $O - Cu - O$ dumbbells parallel to the z axis, and a layer of M-centered octahedra in the xy planes. The stacking follows an ABCABC pattern, forming a rhombohedral Bravais lattice with a space group $R\underline{3}m$ (a trigonal system, symmetry number 166). Table 3 summarizes the optimized lattice parameters for all the studied structures.

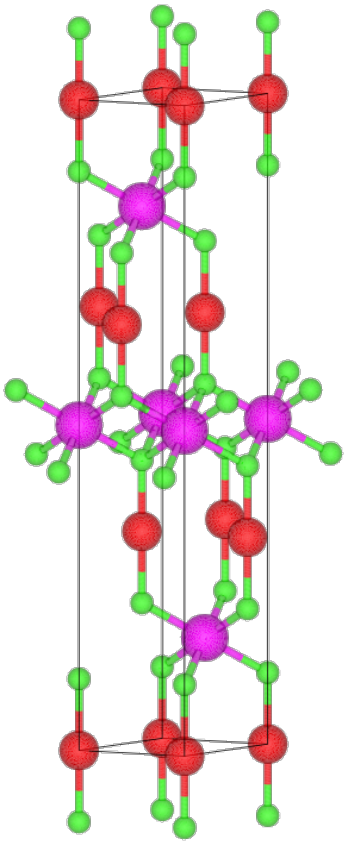

Figure 11: Trigonal structure of the studied delafossite-type semiconductors with the form $CuMO_2$. In this Figure, Cu atoms are shown in red; O atoms are shown in green, and the metal atoms M in pink.
The cell presented corresponds to $CuAlO_2$, and the structure is the same for the rest of the simulated semiconductors, varying only the cell parameters as shown in Table 3.

Table 3: Lattice parameters a and c for the trigonal cells, and volume cell for the studied materials.

Delafossite	a (Å)	c (Å)	Cell volume (Å³)
$CuAlO_2$	2.87	17.05	121.5
$CuCoO_2$	2.86	16.98	120.1
$CuNiO_2$	2.92	16.92	125.5
$CuFeO_2$	2.98	17.35	133.4
$CuGaO_2$	2.97	17.22	131.6
$CuCrO_2$	2.98	17.10	131.3

Table 4 summarizes the bandgap values obtained from our simulations and the optical measurements from Figure 10. It also shows other experimental values found in the literature. Including hybrid functionals allows the possibility of avoiding the typical underestimation of gaps in pure DFT approaches while computational costs remain reasonable. All of these are indirect bandgaps and range from $2-3.5\,eV$ in good agreement with previously reported theoretical simulations and the current experimental results.

Table 4: Bandgap values (in eV) obtained by HSE simulations in comparison with literature and experimental study.

Materials	Bandgap (eV)		
	Literature	DFT	Experimental
$CuAlO_2$	1.9-3.4 [62]–[64]	3.39	2.65
$CuCoO_2$	3.65 [65]	2.18	2.99
$CuNiO_2$	1.41-3.01 [66]–[68]	2.65	2.3
$CuFeO_2$	1.43-3.2 [69], [70]	1.36	2.45
$CuGaO_2$	2.42-3.58 [64], [71]	2.32	2.51
$CuCrO_2$	1.93-3.09 [72]–[74]	2.85	2.75

Figure 12a shows the total and element projected density of states (DOS) for $CuAlO_2$ delafossite. The valence band edge shows a well-defined peak dominated by $Cu-3d$ states, while the rest of this upper part of the valence band also has contributions from $Cu-3d$ states and a large dispersion of $O-2p$ states. The conduction band minimum shows almost equal contributions from Cu and O states.

The $CuAlO_2$ shows a reasonably large bandgap above $3\ eV$, making it transparent in the visible region. Our theoretical result is in good agreement with previously reported values. Table 5 compares the bandgap values obtained for the $CuAlO_2$ in our simulations with values obtained using different hybrid functionals. It can be seen these calculated gaps range from $2.8\ eV$ with an sX-LDA, which is expected to underestimate the gaps due to the LDA contribution, to $3.9\ eV$ the highest value reported. In particular, the three HSE reported values (our HSE06 and the two referenced HSE03 and HSE06) seem to agree in a smaller range of values from $3.1-3.6\ eV$.

Table 5. Bandgap values (in eV) of $CuAlO_2$ obtained by simulations using different hybrid functionals. All the values are for indirect bandgaps.

	$E_{gap}\ (eV)$
HSE06 (our simulation)	3.39
sX-LDA [75]	2.8
HSE03 [76]	3.1
HSE06 [76]	3.6
B3LYP [77]	3.9

Figure 12e shows the DOS for $CuGaO_2$, which is very similar to the previously discussed, but with a considerably lower bandgap value. The valence band edge comes mainly from $Cu-3d$ atoms, as described before, and the rest of the band shows the presence of $Cu-3d$ states, with little contribution from Ga and O states showing a wide dispersion in this region. Despite these similarities, the bandgap value is smaller than the one from $CuAlO_2$ and smaller than others found in the literature [76], [77]. It deviates from the expected result, which should be similar to $CuAlO_2$ as the density of states. However, the experimental bandgap in Figure 10 is similar to our

simulated result. Also, the one reported in Ref. [77] with hybrid functionals HSE, which includes a $CuAlO_2$ bandgap, is in good agreement with ours.

In the $CuCoO_2$ (Fig. 12b), the valence band shows a different composition. The edge remains dominated by $Cu-3d$ states, and O states continue showing a wide dispersion through the band, but the presence of $Co-3d$ states is high in this region, and except for the peak at the edge of the band, is comparable with the contribution from Cu states. Also, the first peak in the conduction band is mainly due to $Co-3d$ states followed by a second peak similar to the one found in $CuAlO_2$ and $CuGaO_2$.

The total and element projected DOS for $CuCrO_2$(c), $CuFeO_2$(d) and $CuNiO_2$(f) are also shown in Figure 12. These compounds have magnetization properties; therefore, spin-polarized simulations were performed. The DOS is split into the majority and minority spin contributions, noted up and down, and plotted in solid and dotted lines, respectively.

$CuCrO_2$ valence band shows, both in the majority and minority spin DOS, an edge dominated by $Cu-3d$ atoms as in the previous compounds. In the majority spin structure, the rest of the band shows strong contributions from Cu and Cr states, and the Cr states are located in a higher energy than those of the Cu. The minority spin structure is mainly due to Cu states. On the other hand, the conduction band's first peaks are mainly due to the Cr states in both minority and majority spin cases.

In $CuFeO_2$ and $CuNiO_2$ the differences in the DOS distribution in the majority and minority spin are visibly more important. Also, it's no more evident that the edge of the valence band is mainly due to the Cu states, especially in $CuNiO_2$. The conduction band firsts peaks for these two elements are dominated by Cu states in the majority spin configuration and by $Ni/Fe-3d$ states in the minority spin configuration. The obtained DOS for $CuFeO_2$ is in good agreement with the ones obtained in Ref. [78] for the bandgap value and the position of Fe peaks in the valence band.

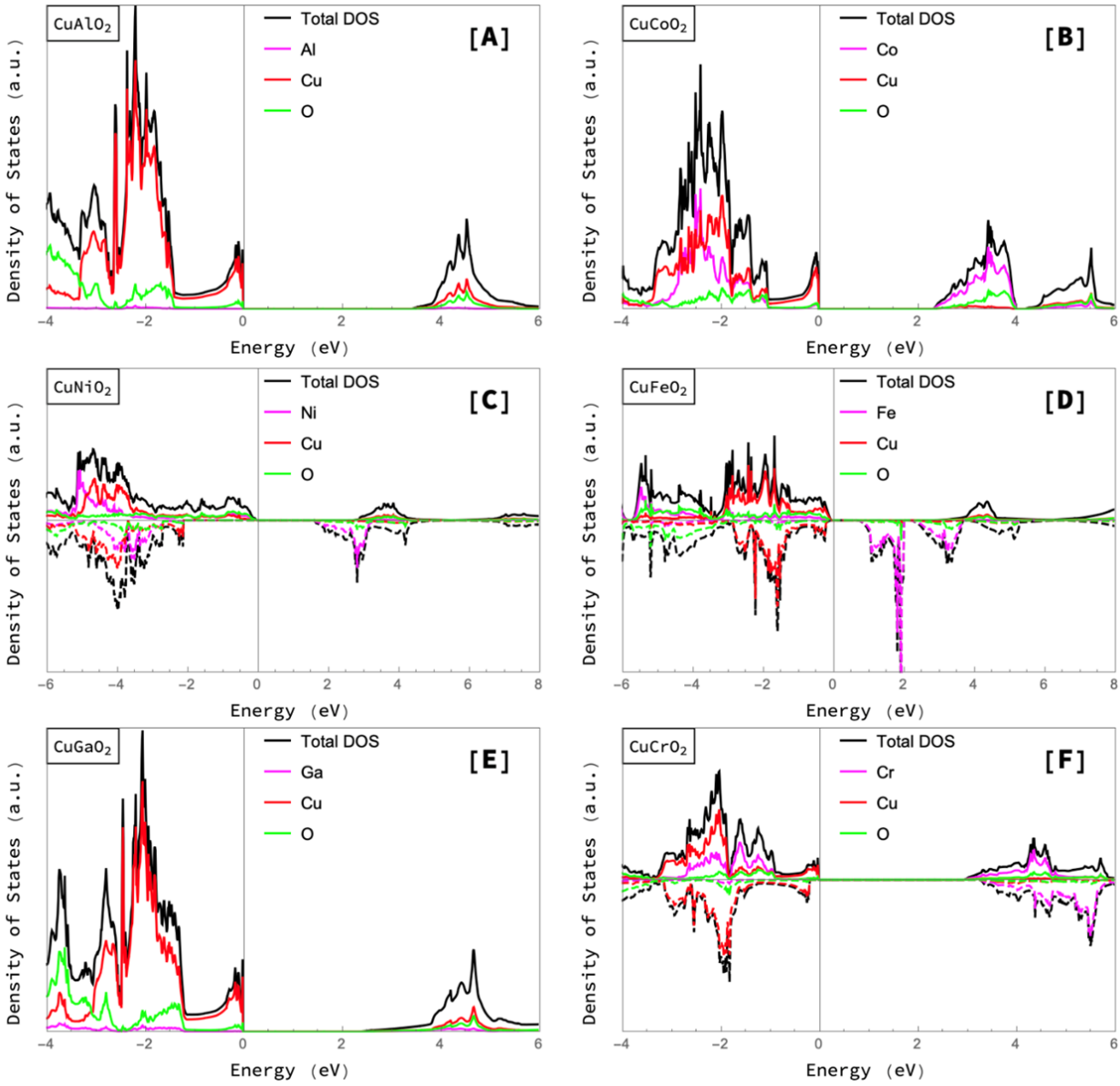

Figure 12: Density of states obtained by HSE simulations for $CuAlO_2$(a), $CuCoO_2$(b), $CuNiO_2$(c), $CuFeO_2$(d), $CuGaO_2$(e) y $CuCrO_2$(f). Black line accounts for total DOS, and colored lines follow the order given in Figure 12: red for Cu atoms, green for O atoms and pink for the M metal atoms. In the case of spin polarized materials, solid lines show the DOS for the majority spin configuration and dashed lines for the minority spin configuration.

5. SCAPS Device Modeling

After having a detailed characterization of delafossite layers using experimental and DFT studies, we further study the effect of these devices in SCAPS-1D software. This was done to analyze that delafossite materials can be used as an alternative to hole transport layers (HTL). this simulation results is based on delafossite band gaps, absorption profiles, mobility and band alignment with absorber and back contact layer.

For this, we simulate standard structure perovskite solar cell in SCAPS-1D (HTL / $Absorber$ / ETL). In this standard perovskite solar cell structure, ETL layer was TiO_2 , Absorber layer is

$MAPbI_3$;The reason for the selection of MA cation is due the high efficiency of $MAPbI_3$ based solar cells and the relevant data regarding this material like experimental band gap and absorption coefficient. For HTL layer is $Spiro - OMeTAD$. Now to analyze the effect of different delafossite layers on solar cell $J - V$ and quantum efficiency (QE%) characteristics, we replace $Spiro - MeoTAD$ with all the characterized delafossite layers in SCAPS-1D by incorporating their physical parameters as drawn in Table 6 and absorption profile extracted from our experiment. the results presented in this work for delafossite materials is based on numerical assumption. And this assumption was taken as by fixing defects density in delafossite layer equal to that of spiro-OMeTAD layer. For analysis we only changes delafossite layer thickness (achieved experimentally), band gap, achieved absorption profile and mobility of carriers. This was done by simply replacing spiro layer with each of delafossite layers and simply by changing those parameters discussed above.

Table 6. Physical input parameters used in the simulation. [79][65]–[68], [71]–[74], [80][81][82]

Parameters	$CuAlO_2$	$CuCoO_2$	$CuNiO_2$	$CuFeO_2$	$CuGaO_2$	$CuCrO_2$
$W\ (nm)$	200	200	210	200	225	210
$E_g\ (eV)$	2.65	2.99	2.2	2.45	2.51	2.75
$\chi\ (eV)$	2.43 [83]	2.3 [84]	3.3 [85]	2.65 [69]	3.1 [64]	2.99 [86]
$N_c(cm^{-3})$	1×10^{19}	1×10^{19}	1×10^{19}	1×10^{19}	1×10^{19}	1×10^{19}
$N_v\ (cm^{-3})$	1×10^{19}	1×10^{19}	1×10^{19}	1×10^{19}	1×10^{19}	1×10^{19}
$n, p\ (cm^{-3})$	1×10^{19}	1×10^{19}	1×10^{19}	1×10^{19}	1×10^{19}	1×10^{19}
$\mu_e\ (cm^2/Vs)$	11.3	0.6	1	0.64	0.2	0.15
$\mu_p\ (cm^2/Vs)$	11.3	0.6	1	0.64	0.2	0.15

The JV result for different delafossite layers is drawn in Figure 13 and Figure 14. The drawn Figure shows that each layer has its JV characteristics. From Figure 13, it is clear that $CuGaO_2$ delafossite has good results in comparison to other layers. The reason for no difference in QE graphs for different devices is because the reelection is not take in the account while simulating solar cell in SCAPS-1D environment. The calculated J_{sc} is well in the range of experimental solar cells [87]–[93].

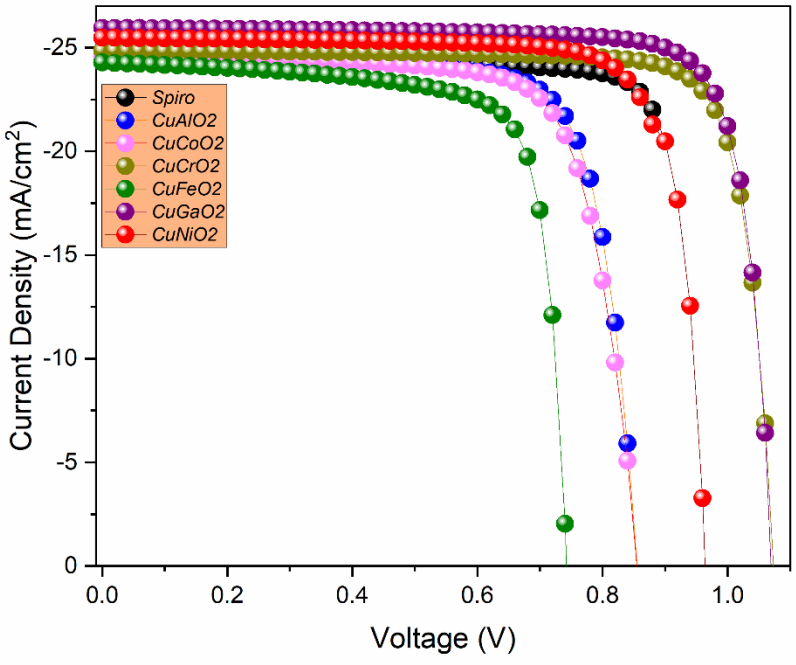

Figure 13: JV characteristics of solar cell having different delafossite layers along with spiro-OMeTAD layer.

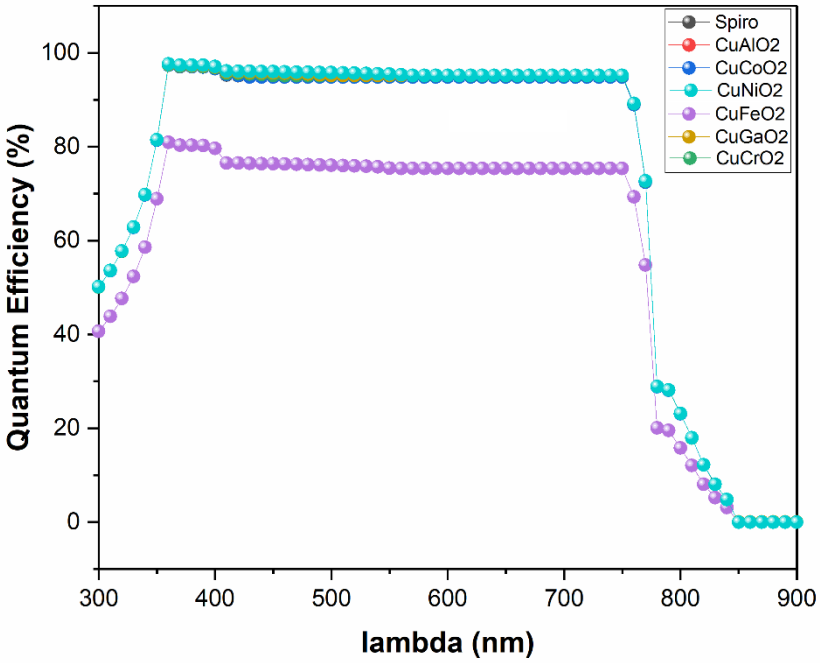

Figure 14: Quantum efficiency of HTL layers

The major reason for this change in device characteristics is their band alignment with the absorber layer. As discussed in our previous work [7], [32], [94], [95] that conduction band offset between ETL/Absorber and valence band offset (VBO) between Absorber/HTL plays an important role in enhancing device efficiency.

Normally at Absorber/HTL, there are two types of band interfaces that occur

- Cliff (+ VBO)
- Spike (-VBO)

The cliff-like band interface will lead to interface recombination at the absorber/HTL layer because the weak built-in potential and higher value of cliff offset will lead to a high

recombination current at the interface. In contrast, in spike-like band offset, we had high built-in potential, which will lead to good charge separation between absorber/HTL layer, thus resulting in higher conversion efficiency for solar cells. Still, a higher spike value will result in high impedance at the interface, which is undesirable in solar cells. Therefore, a moderate spike value at the interface is desirable to achieve a good conversion efficiency from the solar cell. This is shown with the aid of a band diagram and capsule plot for relating interface recombination with a valence band offset at the $MAPbI_3/Delafossite$ in Figure 15 and Figure 16. From Figure 15 band diagram, delafossite materials ($CuAlO_2, CuCoO_2, CuFeO_2$) offered a cliff-like band offset have a higher interface recombination current with respect to others, as drawn in Figure 16, thus limiting the device efficiency.

In contrast, devices with spike-like interfaces have a higher conversion rate ($CuNiO_2$, $CuCrO_2$, $CuGaO_2$). Among these delafossite materials ($CuGaO_2$) is proven to be a promising candidate to be used as an HTL layer by offering the highest Power conversion efficiency (PCE) with respect to other devices. This is because the spike that ($CuGaO_2$) introduce at the interface is quite moderate and suitable for the fabrication of perovskite-based solar cell. The PCE for all the devices are shown in Table 7.

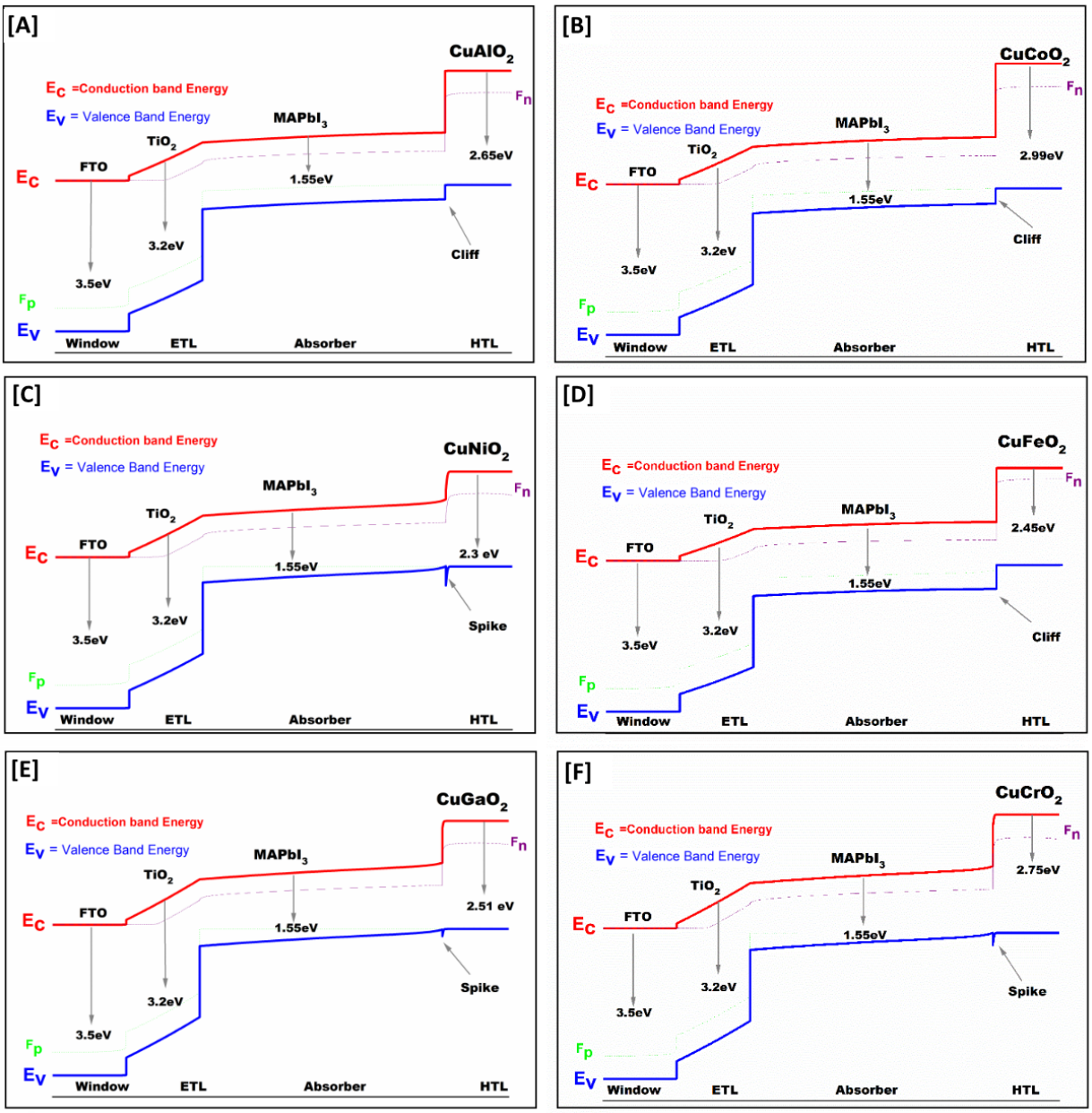

Figure 15: Band diagrams of solar cell structures

Table 7: PCE for all solar cell structures.

Structure	V_{oc} (V)	J_{sc} (mA/cm^2)	FF (%)	PCE (%)
$Spiro-OMeTAD\ /\ MAPbI_3\ /\ TiO_2$	0.94	24.55	82.98	19.65
$CuAlO_2\ /\ MAPbI_3\ /\ TiO_2$	0.86	24.59	76.88	16.18
$CuCoO_2\ /\ MAPbI_3\ /\ TiO_2$	0.85	24.57	74.79	15.79
$CuNiO_2\ /\ MAPbI_3\ /\ TiO_2$	1.07	25.47	72.87	19.71
$CuFeO_2\ /\ MAPbI_3\ /\ TiO_2$	0.74	24.27	77. 33	13.94
$CuGaO_2\ /\ MAPbI_3\ /\ TiO_2$	1.07	25.96	82.42	22.90
$CuCrO_2\ /\ MAPbI_3\ /\ TiO_2$	1.07	24.86	82.70	22.08

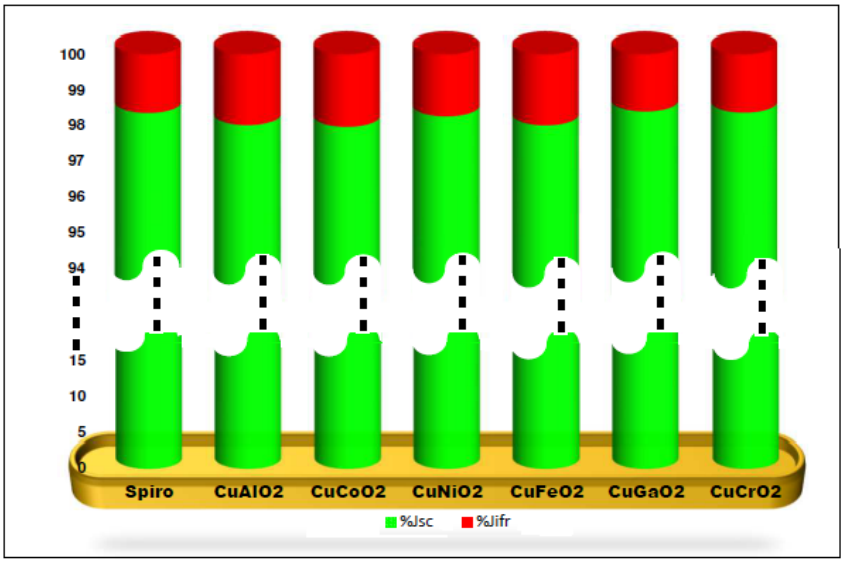

Figure 16: Capsule plot for interface recombination due to different band structures

Conclusion:

As a result of this work, we propose a successful technique to manufacture delafossite materials that can be used as Hole Transport Layers (HTLs) in organic lead halide Perovskite solar cells (PSCs). Several types of $CuMO_2$ delafossite were examined for their crystal structure, morphology, and optical properties influenced by the M cation. Delafossite layers can be seen on the XRD and SEM images, which confirms the hexagonal and rhombohedral structure of the crystals. The optical band gap ranges from 2.2eV to 2.99eV. We also perform density functional theory (DFT) calculations for delafossite layers to determine their electronic properties. Using experimental results and DFT calculations, we used SCAPS-1D software to perform numerical analysis on standard solar cell structures and replace them with all the deposited delafossite layers. As a result of our numerical analysis, the $CuGaO_2$ HTL shows the highest power conversion efficiency (PCE%) of 22.90. This finding could provide a good direction for manufacturing Perovskite-based solar cells (PSCs) with improved performance.

Acknowledgments:

This work has been funded by the Spanish Agencia Estatal de Investigación (grants BESTMAT PID2019-107137RB-C21/AEI/10.13039/501100011033 and PID2019-107137RB-C22/AEI/10.13039/ 501100011033), the Generalitat valenciana (grant AGPIDI/2022/46/009) and by ERDF under the funding “A way of making Europe”. The author Amal Bouich acknowledges the Ministerio de Ciencia e Innovación for funding support through Margarita Salas Fellowship (MCIN/AEI/10.13039/501100011033).

References:

[1] R. Sharma, A. Sharma, S. Agarwal, and M. S. Dhaka, "Stability and efficiency issues, solutions and advancements in perovskite solar cells: A review," *Sol. Energy*, vol. 244, pp. 516–535, Sep. 2022.

[2] H. Zhang, X. Ji, H. Yao, Q. Fan, B. Yu, and J. Li, "Review on efficiency improvement effort of perovskite solar cell," *Sol. Energy*, vol. 233, pp. 421–434, Feb. 2022.

[3] B. Roose *et al.*, "Local manufacturing of perovskite solar cells, a game-changer for low- and lower-middle income countries?," *Energy Environ. Sci.*, vol. 15, no. 9, pp. 3571–3582, 2022.

[4] B. Lipovšek, M. Jošt, Š. Tomšič, and M. Topič, "Energy yield of perovskite solar cells: Influence of location, orientation, and external light management," *Sol. Energy Mater. Sol. Cells*, vol. 234, p. 111421, Jan. 2022.

[5] S. Asgharizadeh and S. Khesali Azadi, "Additive MXene and dominant recombination channel in perovskite solar cells," *Sol. Energy*, vol. 241, pp. 720–727, Jul. 2022.

[6] M. Wang, C. Fei, M. A. Uddin, and J. Huang, "Influence of voids on the thermal and light stability of perovskite solar cells," *Sci. Adv.*, vol. 8, no. 38, Sep. 2022.

[7] Q. Jiang *et al.*, "Surface reaction for efficient and stable inverted perovskite solar cells," *Nature*, vol. 611, no. 7935, pp. 278–283, Nov. 2022.

[8] Q. Zhuang *et al.*, "Tailoring multifunctional anion modifiers to modulate interfacial chemical interactions for efficient and stable perovskite solar cells," *Nano Energy*, vol. 102, p. 107747, Nov. 2022.

[9] M. K. A. Mohammed *et al.*, "Ionic Liquid Passivator for Mesoporous Titanium Dioxide Electron Transport Layer to Enhance the Efficiency and Stability of Hole Conductor-Free Perovskite Solar Cells," *Energy & Fuels*, vol. 36, no. 19, pp. 12192–12200, Oct. 2022.

[10] Y. Jiang *et al.*, "Reducing Energy Disorder in Perovskite Solar Cells by Chelation," *J. Am. Chem. Soc.*, vol. 144, no. 12, pp. 5400–5410, Mar. 2022.

[11] S. Yun *et al.*, "New-generation integrated devices based on dye-sensitized and perovskite solar cells," *Energy Environ. Sci.*, vol. 11, no. 3, pp. 476–526, 2018.

[12] A. P. Mackenzie, "The properties of ultrapure delafossite metals," *Reports Prog. Phys.*, vol. 80, no. 3, p. 032501, Mar. 2017.

[13] M. A. Marquardt, N. A. Ashmore, and D. P. Cann, "Crystal chemistry and electrical properties of the delafossite structure," *Thin Solid Films*, vol. 496, no. 1, pp. 146–156, Feb. 2006.

[14] W. C. Sheets, E. Mugnier, A. Barnabé, T. J. Marks, and K. R. Poeppelmeier, "Hydrothermal Synthesis of Delafossite-Type Oxides," *Chem. Mater.*, vol. 18, no. 1, pp. 7–20, Jan. 2006.

[15] R. Nagarajan *et al.*, "p-Type conductivity in the delafossite structure," *Int. J. Inorg. Mater.*, vol. 3, no. 3, pp. 265–270, Jun. 2001.

[16] H. Ohta and H. Hosono, "Transparent oxide optoelectronics," *Mater. Today*, vol. 7, no. 6, pp. 42–51, Jun. 2004.

[17] R. A. Afre, N. Sharma, M. Sharon, and M. Sharon, "Transparent Conducting Oxide Films for Various Applications: A Review," *Rev. Adv. Mater. Sci.*, vol. 53, no. 1, pp. 79–89, Jan. 2018.

[18] P. Würfel, *Physics of Solar Cells*. Wiley, 2005.

[19] E. Schiavo, C. Latouche, V. Barone, O. Crescenzi, A. B. Muñoz-García, and M. Pavone, "An ab initio study of Cu-based delafossites as an alternative to nickel oxide in photocathodes: effects of Mg-doping and surface electronic features," *Phys. Chem. Chem. Phys.*, vol. 20, no. 20, pp. 14082–14089, 2018.

[20] A. Buljan, P. Alemany, and E. Ruiz, "Electronic Structure and Bonding in CuMO 2 (M = Al, Ga, Y) Delafossite-Type Oxides: An Ab Initio Study," *J. Phys. Chem. B*, vol. 103, no. 38, pp. 8060–8066, Sep. 1999.

[21] Y. Pu *et al.*, "First-principles screening visible-light active delafossite ABO2 structures for photocatalytic application," *Int. J. Hydrogen Energy*, vol. 43, no. 36, pp. 17271–17282, Sep. 2018.

[22] C. Baiano *et al.*, "Role of surface defects in CO2 adsorption and activation on CuFeO2 delafossite oxide," *Mol. Catal.*, vol. 496, p. 111181, Nov. 2020.

[23] J. Ahmed and Y. Mao, "Synthesis, characterization and electrocatalytic properties of delafossite CuGaO2," *J. Solid*

State Chem., vol. 242, pp. 77–85, Oct. 2016.

[24] J. Pellicer-Porres, A. Segura, and D. Kim, "Refractive index of the CuAlO 2 delafossite," *Semicond. Sci. Technol.*, vol. 24, no. 1, p. 015002, Jan. 2009.

[25] N. Sahu, B. Parija, and S. Panigrahi, "Fundamental understanding and modeling of spin coating process: A review," *Indian J. Phys.*, vol. 83, no. 4, pp. 493–502, Apr. 2009.

[26] W. O. Herrera Martínez, N. B. Correa Guerrero, V. A. Gómez Andrade, M. Alurralde, and M. D. Perez, "Evaluation of the resistance of halide perovskite solar cells to high energy proton irradiation for space applications," *Sol. Energy Mater. Sol. Cells*, vol. 238, p. 111644, May 2022.

[27] Y. Lao *et al.*, "Highly efficient perovskite solar cells enhanced by biphenyl-4,4-dithiol," *Sol. Energy Mater. Sol. Cells*, vol. 235, p. 111462, Jan. 2022.

[28] Z. Shi *et al.*, "Light Management through Organic Bulk Heterojunction and Carrier Interfacial Engineering for Perovskite Solar Cells with 23.5% Efficiency," *Adv. Funct. Mater.*, vol. 32, no. 35, p. 2203873, Aug. 2022.

[29] S. Mandati, R. Dileep. k, G. Veerappan, and E. Ramasamy, "Large area bar coated TiO2 electron transport layers for perovskite solar cells with excellent performance homogeneity," *Sol. Energy*, vol. 240, pp. 258–268, Jul. 2022.

[30] J. Bi *et al.*, "A Highly integrated flexible photo-rechargeable system based on stable ultrahigh-rate quasi-solid-state zinc-ion micro-batteries and perovskite solar cells," *Energy Storage Mater.*, vol. 51, pp. 239–248, Oct. 2022.

[31] P. Yan, D. Yang, H. Wang, S. Yang, and Z. Ge, "Recent advances in dopant-free organic hole-transporting materials for efficient, stable and low-cost perovskite solar cells," *Energy Environ. Sci.*, vol. 15, no. 9, pp. 3630–3669, 2022.

[32] B. Huang, X. Xia, X. Wang, and F. Li, "Surface treatment enabled by functional guanidinium tetrafluoroborate achieving high-performance inverted perovskite solar cells," *Sol. Energy Mater. Sol. Cells*, vol. 240, p. 111682, Jun. 2022.

[33] K. Murugan, A. T. Sathyanarayana, P. Govindaraj, S. Paulraj, A. Mani, and K. Venugopal, "Investigating the Magnetocaloric Properties of Magnetically Frustrated Delafossite: AgCrO2," *J. Electron. Mater.*, Oct. 2022.

[34] R. Jeyakumar and A. Bag, "Performance evaluation and optimization of CH3NH3PbBr3 based planar perovskite solar cells using various hole-transport layers," *Sol. Energy*, vol. 236, pp. 832–840, Apr. 2022.

[35] J. H. Heo *et al.*, "Surface engineering with oxidized Ti3C2Tx MXene enables efficient and stable p-i-n-structured CsPbI3 perovskite solar cells," *Joule*, vol. 6, no. 7, pp. 1672–1688, Jul. 2022.

[36] S. H. Reddy, F. Di Giacomo, and A. Di Carlo, "Low-Temperature-Processed Stable Perovskite Solar Cells and Modules: A Comprehensive Review," *Adv. Energy Mater.*, vol. 12, no. 13, p. 2103534, Apr. 2022.

[37] Z. Liu, Z. Yang, W. Yang, J. Sheng, Y. Zeng, and J. Ye, "Optical management for back-contact perovskite solar cells with diverse structure designs," *Sol. Energy*, vol. 236, pp. 100–106, Apr. 2022.

[38] N. Naeem, R. A. Shehzad, M. Ans, M. S. Akhter, and J. Iqbal, "Dopant Free Triphenylamine-Based Hole Transport Materials with Excellent Photovoltaic Properties for High-Performance Perovskite Solar Cells," *Energy Technol.*, vol. 10, no. 2, p. 2100838, Feb. 2022.

[39] A. M. Asiri *et al.*, "Solar Water Splitting Using Earth-Abundant Electrocatalysts Driven by High-Efficiency Perovskite Solar Cells," *ChemSusChem*, vol. 15, no. 4, Feb. 2022.

[40] M. Yu, G. Natu, Z. Ji, and Y. Wu, "p-Type Dye-Sensitized Solar Cells Based on Delafossite CuGaO 2 Nanoplates with Saturation Photovoltages Exceeding 460 mV," *J. Phys. Chem. Lett.*, vol. 3, no. 9, pp. 1074–1078, May 2012.

[41] J. W. Lekse, M. K. Underwood, J. P. Lewis, and C. Matranga, "Synthesis, Characterization, Electronic Structure, and Photocatalytic Behavior of CuGaO 2 and CuGa 1– x Fe x O 2 (x = 0.05, 0.10, 0.15, 0.20) Delafossites," *J. Phys. Chem. C*, vol. 116, no. 2, pp. 1865–1872, Jan. 2012.

[42] C. G. Read, Y. Park, and K.-S. Choi, "Electrochemical Synthesis of p-Type CuFeO 2 Electrodes for Use in a Photoelectrochemical Cell," *J. Phys. Chem. Lett.*, vol. 3, no. 14, pp. 1872–1876, Jul. 2012.

[43] J. Gu *et al.*, "Mg-Doped CuFeO 2 Photocathodes for Photoelectrochemical Reduction of Carbon Dioxide," *J. Phys. Chem. C*, vol. 117, no. 24, pp. 12415–12422, Jun. 2013.

[44] Y. J. Jang, Y. Bin Park, H. E. Kim, Y. H. Choi, S. H. Choi, and J. S. Lee, "Oxygen-Intercalated CuFeO 2 Photocathode Fabricated by Hybrid Microwave Annealing for Efficient Solar Hydrogen Production," *Chem. Mater.*, vol. 28, no. 17,

pp. 6054–6061, Sep. 2016.

[45] H. Zhang *et al.*, "Low-Temperature Solution-Processed CuCrO 2 Hole-Transporting Layer for Efficient and Photostable Perovskite Solar Cells," *Adv. Energy Mater.*, vol. 8, no. 13, p. 1702762, May 2018.

[46] A. Bouich *et al.*, "Experimental, theoretical, and numerical simulation of the performance of CuInxGa(1-x) S2-based solar cells," *Optik (Stuttg).*, vol. 183, pp. 137–147, Apr. 2019.

[47] A. W. Stewart, A. Bouich, and B. Marí, "Inorganic perovskites improved film and crystal quality of CsPbIBr2 when doped with rubidium," *J. Mater. Sci. Mater. Electron.*, vol. 32, no. 20, pp. 24825–24833, Oct. 2021.

[48] K. Koumoto, H. Koduka, and W.-S. Seo, "Thermoelectric properties of single crystal CuAlO2 with a layered structure," *J. Mater. Chem.*, vol. 11, no. 2, pp. 251–252, 2001.

[49] B. J. Inkson, "Scanning electron microscopy (SEM) and transmission electron microscopy (TEM) for materials characterization," in *Materials Characterization Using Nondestructive Evaluation (NDE) Methods*, Elsevier, 2016, pp. 17–43.

[50] T. Maitland and S. Sitzman, "Backscattering Detector and EBSD in Nanomaterials Characterization," in *Scanning Microscopy for Nanotechnology*, New York, NY: Springer New York, 2006, pp. 41–75.

[51] M. A. Haque and M. T. A. Saif, "Application of MEMS force sensors for in situ mechanical characterization of nano-scale thin films in SEM and TEM," *Sensors Actuators A Phys.*, vol. 97–98, pp. 239–245, Apr. 2002.

[52] T. L. Gilbert, "Hohenberg-Kohn theorem for nonlocal external potentials," *Phys. Rev. B*, vol. 12, no. 6, pp. 2111–2120, Sep. 1975.

[53] A. Seidl, A. Görling, P. Vogl, J. A. Majewski, and M. Levy, "Generalized Kohn-Sham schemes and the band-gap problem," *Phys. Rev. B*, vol. 53, no. 7, pp. 3764–3774, Feb. 1996.

[54] P. E. Blöchl, "Projector augmented-wave method," *Phys. Rev. B*, vol. 50, no. 24, pp. 17953–17979, Dec. 1994.

[55] A. V. Krukau, O. A. Vydrov, A. F. Izmaylov, and G. E. Scuseria, "Influence of the exchange screening parameter on the performance of screened hybrid functionals," *J. Chem. Phys.*, vol. 125, no. 22, p. 224106, Dec. 2006.

[56] J. Heyd, G. E. Scuseria, and M. Ernzerhof, "Hybrid functionals based on a screened Coulomb potential," *J. Chem. Phys.*, vol. 118, no. 18, pp. 8207–8215, May 2003.

[57] J. Heyd and G. E. Scuseria, "Assessment and validation of a screened Coulomb hybrid density functional," *J. Chem. Phys.*, vol. 120, no. 16, pp. 7274–7280, Apr. 2004.

[58] G. Kresse and J. Hafner, "Ab initio molecular dynamics for open-shell transition metals," *Phys. Rev. B*, vol. 48, no. 17, pp. 13115–13118, Nov. 1993.

[59] G. Kresse and J. Furthmüller, "Efficient iterative schemes for ab initio total-energy calculations using a plane-wave basis set," *Phys. Rev. B*, vol. 54, no. 16, pp. 11169–11186, Oct. 1996.

[60] G. Kresse and D. Joubert, "From ultrasoft pseudopotentials to the projector augmented-wave method," *Phys. Rev. B*, vol. 59, no. 3, pp. 1758–1775, Jan. 1999.

[61] H. J. Monkhorst and J. D. Pack, "Special points for Brillouin-zone integrations," *Phys. Rev. B*, vol. 13, no. 12, pp. 5188–5192, Jun. 1976.

[62] N. N. Som, V. Sharma, V. Mankad, M. L. C. Attygalle, and P. K. Jha, "Role of CuAlO2 as an absorber layer for solar energy converter," *Sol. Energy*, vol. 193, no. September, pp. 799–805, 2019.

[63] Z. Xiong, Z. Li, Y. Yin, C. Pu, T. Zeng, and X. An, "First-Principles Study on Electronic and Optical Properties of Fe Doped α-Bi2O3," *Rengong Jingti Xuebao/Journal Synth. Cryst.*, vol. 50, no. 2, pp. 278–282, 2021.

[64] M.-S. S. Miao, S. Yarbro, P. T. Barton, and R. Seshadri, "Electron affinities and ionization energies of Cu and Ag delafossite compounds: A hybrid functional study," *Phys. Rev. B*, vol. 89, no. 4, p. 045306, Jan. 2014.

[65] C. Ruttanapun, M. Sa-nguan-cheep, S. Kahatta, P. Buranasiri, and P. Jindajitawat, " Optical and electronic transport properties of p -type CuCoO 2 transparent conductive oxide ," *ICPS 2013 Int. Conf. Photonics Solut.*, vol. 8883, no. June 2013, p. 88831O, 2013.

[66] R. Chouhan, A. Agrawal, M. Gupta, and P. Sen, "Qualitative Analysis of the Valence and Conduction Band Offset Parameters in FeNiO/CuNiO Bilayer Film Using X-Ray Photoelectron Spectroscopy," *Phys. Status Solidi Basic Res.*, vol. 259, no. 1, pp. 1–7, 2022.

[67] A. Sreedhar, M. Hari Prasad Reddy, S. Uthanna, and J. F. Pierson, " Sputter Power Influenced Structural, Electrical, and Optical Behaviour of Nanocrystalline CuNiO 2 Films Formed by RF Magnetron Sputtering ," *ISRN Condens. Matter Phys.*, vol. 2013, no. January, pp. 1–9, 2013.

[68] R. K, H. Reddy, and U. S, "Studies on the structural, electrical and optical properties of thermally oxidized copper nickel oxide thin films," *Front. Nanosci. Nanotechnol.*, vol. 3, no. 2, pp. 1–7, 2017.

[69] S. Akin, F. Sadegh, S. Turan, and S. Sonmezoglu, "Inorganic CuFeO2 Delafossite Nanoparticles as Effective Hole Transport Materials for Highly Efficient and Long-Term Stable Perovskite Solar Cells," *ACS Appl. Mater. Interfaces*, vol. 11, no. 48, pp. 45142–45149, 2019.

[70] C. M. Jiang *et al.*, "Electronic Structure and Performance Bottlenecks of CuFeO2 Photocathodes," *Chem. Mater.*, vol. 31, no. 7, pp. 2524–2534, 2019.

[71] H. Zhang, H. Wang, W. Chen, and A. K. Y. Jen, "CuGaO2: A Promising Inorganic Hole-Transporting Material for Highly Efficient and Stable Perovskite Solar Cells," *Adv. Mater.*, vol. 29, no. 8, 2017.

[72] T. S. Tripathi, J. P. Niemelä, and M. Karppinen, "Atomic layer deposition of transparent semiconducting oxide CuCrO2 thin films," *J. Mater. Chem. C*, vol. 3, no. 32, pp. 8364–8371, 2015.

[73] I. Sinnarasa, Y. Thimont, L. Presmanes, A. Barnabé, and P. Tailhades, "Thermoelectric and transport properties of delafossite CuCrO2: Mg thin films prepared by RF magnetron sputtering," *Nanomaterials*, vol. 7, no. 7, 2017.

[74] M. Moreira, J. Afonso, J. Crepelliere, D. Lenoble, and P. Lunca-Popa, "A review on the p-type transparent Cu–Cr–O delafossite materials," *J. Mater. Sci.*, vol. 57, no. 5, pp. 3114–3142, 2022.

[75] F. Trani, J. Vidal, S. Botti, and M. A. L. Marques, "Band structures of delafossite transparent conductive oxides from a self-consistent GW approach," *Phys. Rev. B*, vol. 82, no. 8, p. 085115, Aug. 2010.

[76] R. Gillen and J. Robertson, "Band structure calculations of CuAlO2, CuGaO2, CuInO2 and CuCr)2 by screened exchange," *Phys. Rev. B*, vol. 84, no. 3, p. 035125, Jul. 2011.

[77] J. Robertson, P. . Peacock, M. . Towler, and R. Needs, "Electronic structure of p-type conducting transparent oxides," *Thin Solid Films*, vol. 411, no. 1, pp. 96–100, May 2002.

[78] M. Ferri, J. Elliott, S. Fabris, and S. Piccinin, "Establishing best practices to model the electronic structure of CuFeO2 from first principles," *Phys. Rev. B*, vol. 101, no. 15, p. 155201, Apr. 2020.

[79] Y. H. Khattak, F. Baig, A. Shuja, S. Beg, and B. M. Soucase, "Numerical analysis guidelines for the design of efficient novel nip structures for perovskite solar cell," *Sol. Energy*, vol. 207, pp. 579–591, Sep. 2020.

[80] X. Liu *et al.*, "Thermal Evaporation and Characterization of Sb $_2$ Se $_3$ Thin Film for Substrate Sb $_2$ Se $_3$ /CdS Solar Cells," *ACS Appl. Mater. Interfaces*, vol. 6, no. 13, pp. 10687–10695, 2014.

[81] Y. H. Khattak, F. Baig, A. Shuja, L. Atourki, K. Riaz, and B. M. Soucase, "Device Optimization of PIN Structured Perovskite Solar Cells: Impact of Design Variants," *ACS Appl. Electron. Mater.*, vol. 3, no. 8, pp. 3509–3520, Aug. 2021.

[82] F. Baig, Y. H. Khattak, S. Ullah, B. M. Soucase, S. Beg, and H. Ullah, "Numerical analysis a guide to improve the efficiency of experimentally designed solar cell," *Appl. Phys. A*, vol. 124, no. 7, p. 471, Jul. 2018.

[83] Z. Q. Yao *et al.*, "Energy band engineering and controlled p-type conductivity of CuAlO 2 thin films by nonisovalent Cu-O alloying," *Appl. Phys. Lett.*, vol. 100, no. 6, 2012.

[84] H. Bouakaz, M. Abbas, R. Brahimi, and M. Trari, "Physical properties of the delafossite CuCoO2 synthesized by co-precipitation /hydrothermal route," *Mater. Sci. Semicond. Process.*, vol. 136, no. July, p. 106132, 2021.

[85] S. Shahshahan, "Increased Open Circuit Voltage Using Copper- Based Oxide Semiconductors as Photocathodes in p-Type Dye-Sensitized Solar Cells Sayedmohsen Shahshahan," 2020.

[86] N. Benreguia, A. Abdi, O. Mahroua, and M. Trari, "Semiconducting and photoelectrochemical characterizations of CuCrO2 powder synthesized by sol-gel method," *J. Solid State Electrochem.*, vol. 22, no. 8, pp. 2499–2506, 2018.

[87] T. Wu *et al.*, "The Main Progress of Perovskite Solar Cells in 2020–2021," *Nano-Micro Lett.*, vol. 13, no. 1, p. 152, Dec. 2021.

[88] Y. Li *et al.*, "Over 20% Efficiency in Methylammonium Lead Iodide Perovskite Solar Cells with Enhanced Stability via 'in Situ Solidification' of the TiO 2 Compact Layer," *ACS Appl. Mater. Interfaces*, vol. 12, no. 6, pp. 7135–7143, Feb.

2020.

[89] Y. Yin *et al.*, “Efficient and Stable Ideal Bandgap Perovskite Solar Cell Achieved by a Small Amount of Tin Substituted Methylammonium Lead Iodide,” *Electron. Mater. Lett.*, vol. 16, no. 3, pp. 224–230, May 2020.

[90] P. Singh, R. Mukherjee, and S. Avasthi, “Acetamidinium-Substituted Methylammonium Lead Iodide Perovskite Solar Cells with Higher Open-Circuit Voltage and Improved Intrinsic Stability,” *ACS Appl. Mater. Interfaces*, vol. 12, no. 12, pp. 13982–13987, Mar. 2020.

[91] M. K. A. Mohammed, G. Sarusi, P. Sakthivel, G. Ravi, and U. Younis, “Improved stability of ambient air-processed methylammonium lead iodide using carbon nanotubes for perovskite solar cells,” *Mater. Res. Bull.*, vol. 137, p. 111182, May 2021.

[92] Y. Yun *et al.*, “Intermediate Phase-Free Process for Methylammonium Lead Iodide Thin Film for High-Efficiency Perovskite Solar Cells,” *Adv. Sci.*, vol. 8, no. 21, p. 2102492, Nov. 2021.

[93] E. A. Alharbi *et al.*, “Atomic-level passivation mechanism of ammonium salts enabling highly efficient perovskite solar cells,” *Nat. Commun.*, vol. 10, no. 1, p. 3008, Dec. 2019.

[94] W.-S. Tseng *et al.*, “The effects of interfacial dipole caused by annealing-free Al-doped NiOx in efficient perovskite solar cells,” *Sol. Energy*, vol. 233, pp. 345–352, Feb. 2022.

[95] S. Zhang *et al.*, “Spontaneous Construction of Multidimensional Heterostructure Enables Enhanced Hole Extraction for Inorganic Perovskite Solar Cells to Exceed 20% Efficiency,” *Adv. Energy Mater.*, vol. 12, no. 1, p. 2103007, Jan. 2022.